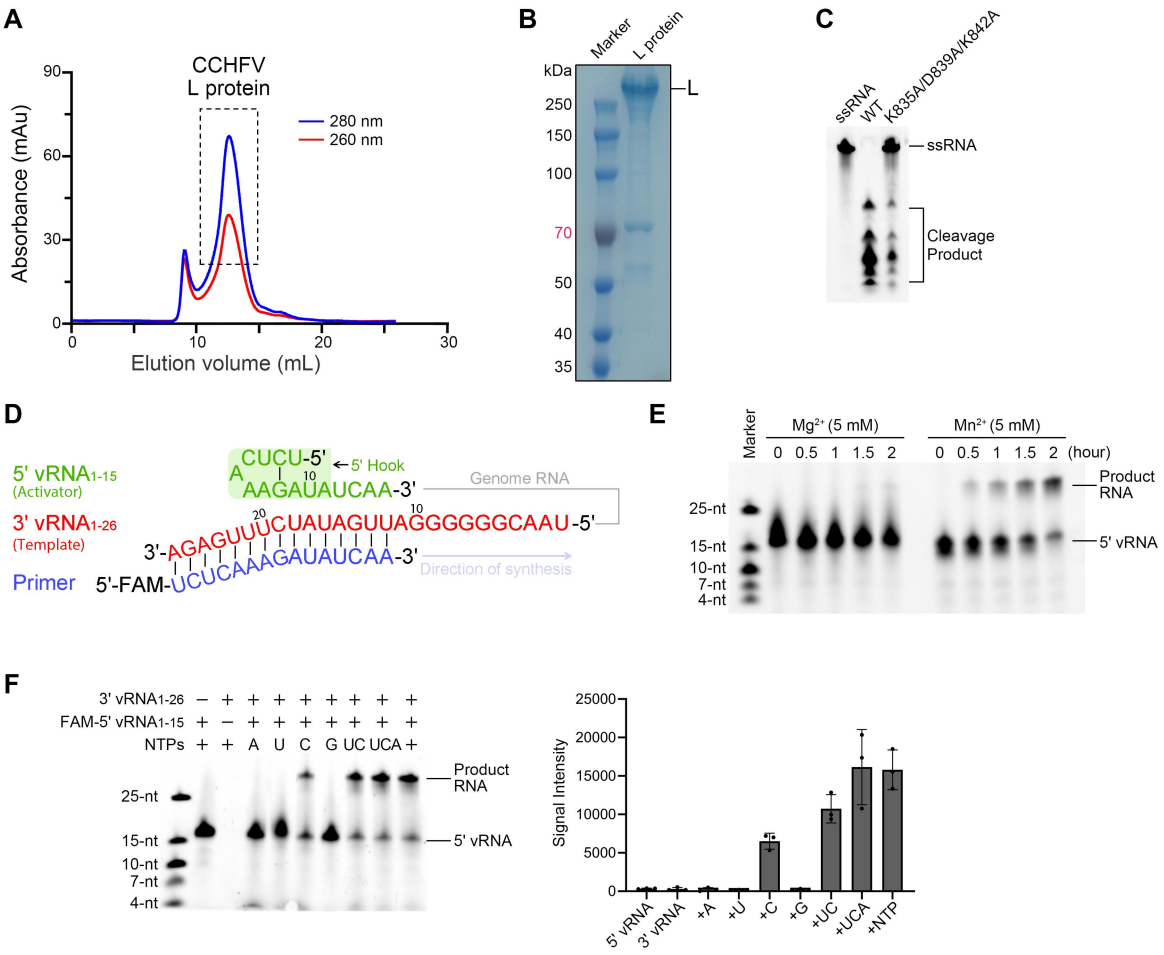

Figure S1. Purification and functional characterization of the CCHFV L protein, related to Figures 1 and 2

(A) Size-exclusion chromatography (SEC) profile of the recombinant CCHFV L protein. The dashed box indicates the fraction collected for structural and functional studies.

(B) SDS-PAGE analysis of the purified L protein, showing a predominant band corresponding to the expected molecular weight (~450 kDa).

(C) Endonuclease activity assay. The wild-type (WT) L protein exhibits robust endonuclease activity against the ssRNA substrate, whereas the activity is abolished in the endonuclease-defective mutant (K835A/D839A/K842A).

(D) Sequences and schematic of the RNA oligonucleotides used in this study. The 15-nt activator (5' vRNA, green) features a conserved "hook" secondary structure. The 5'-FAM-labeled primer (blue) is hybridized to the 26-nt 3' vRNA template (red) to initiate synthesis, indicated by an arrow. Black vertical lines represent intramolecular base pairing within the 5' vRNA hook and intermolecular complementarity between the primer and the template.

(E) Metal ion cofactor evaluation. *In vitro* primer extension assays demonstrate that product RNA synthesis is supported by 5 mM manganese (Mn^{2+}) but is negligible with magnesium (Mg^{2+}) after incubation for up to 2 hours.

(F) Functional verification of the L protein–promoter complex. Left: Primer-extension assays conducted with various NTP combinations. Full-length product synthesis is minimal under CTP (C) alone and moderate under CTP/UTP (UC), whereas peak efficiency strictly requires all complementary NTPs (UCA or full NTPs), confirming template-dependent polymerase activity. Right: Densitometric quantification of the product RNA bands analyzed using ImageJ (mean ± SD). Gel images in (C), (E), and (F) are representative of three independent experiments, with quantitative data representing the summary (n = 3).

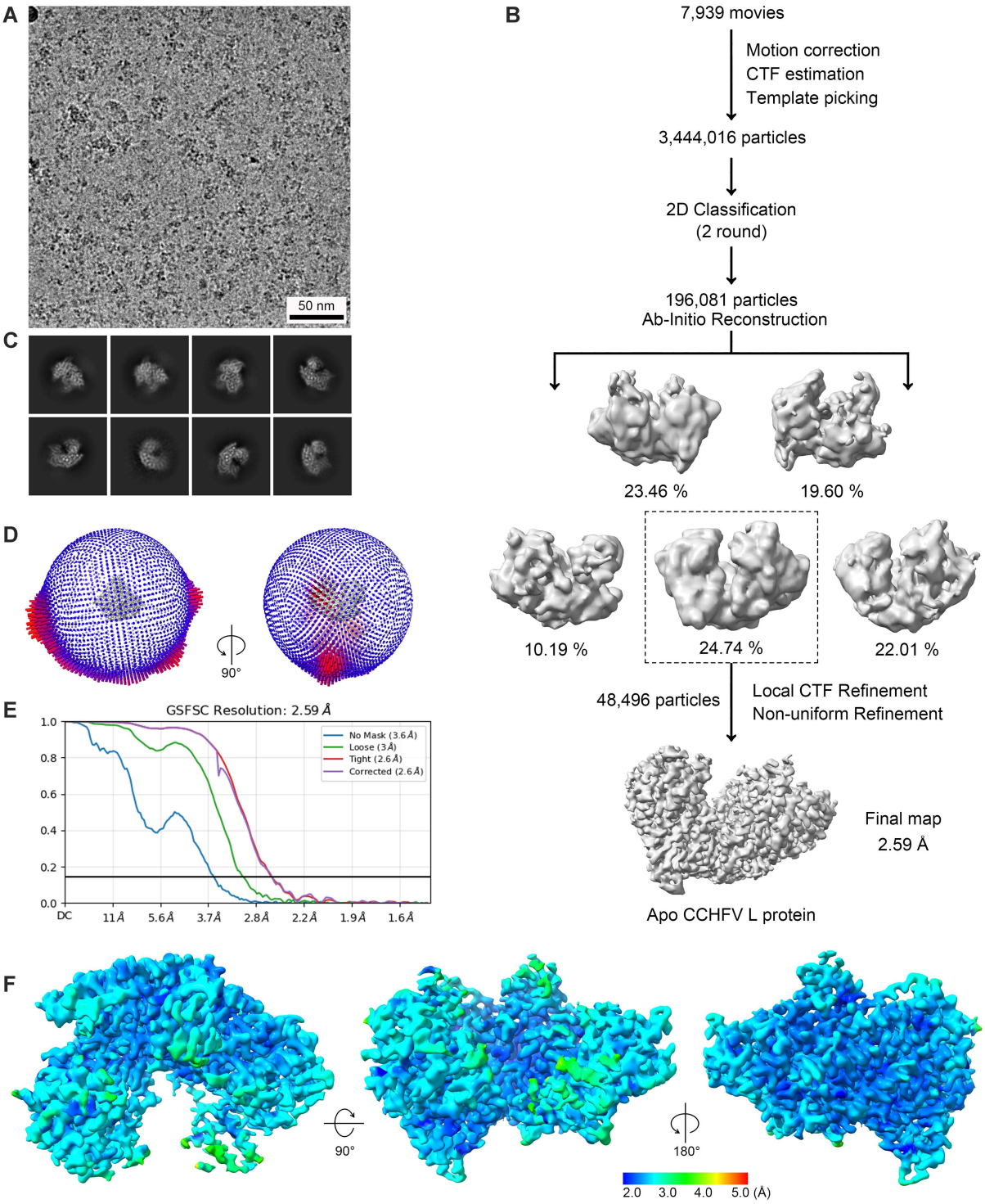

Figure S2. Cryo-EM data processing and reconstruction of apo CCHFV L protein, related to Figure 1

(A) Representative cryo-EM micrograph of the apo CCHFV L protein. Scale bar, 50 nm.

(B) Data processing workflow. A total of 7,939 movies yielded 3,444,016 particles, which were subjected to 2D classification, *ab initio* reconstruction, and heterogeneous refinement to generate a final map from 48,496 particles.

(C) Representative 2D class averages showing distinct orientations of the L protein.

(D) Angular distribution plot of the particles included in the final reconstruction.

(E) Gold-standard Fourier Shell Correlation (FSC) curve indicating a final global resolution of 2.59 Å at the 0.143 criterion.

(F) Local resolution map of the final reconstruction shown in three distinct views, presented in the same orientations as Figures 1B and 1C; the resolution color key is shown below.

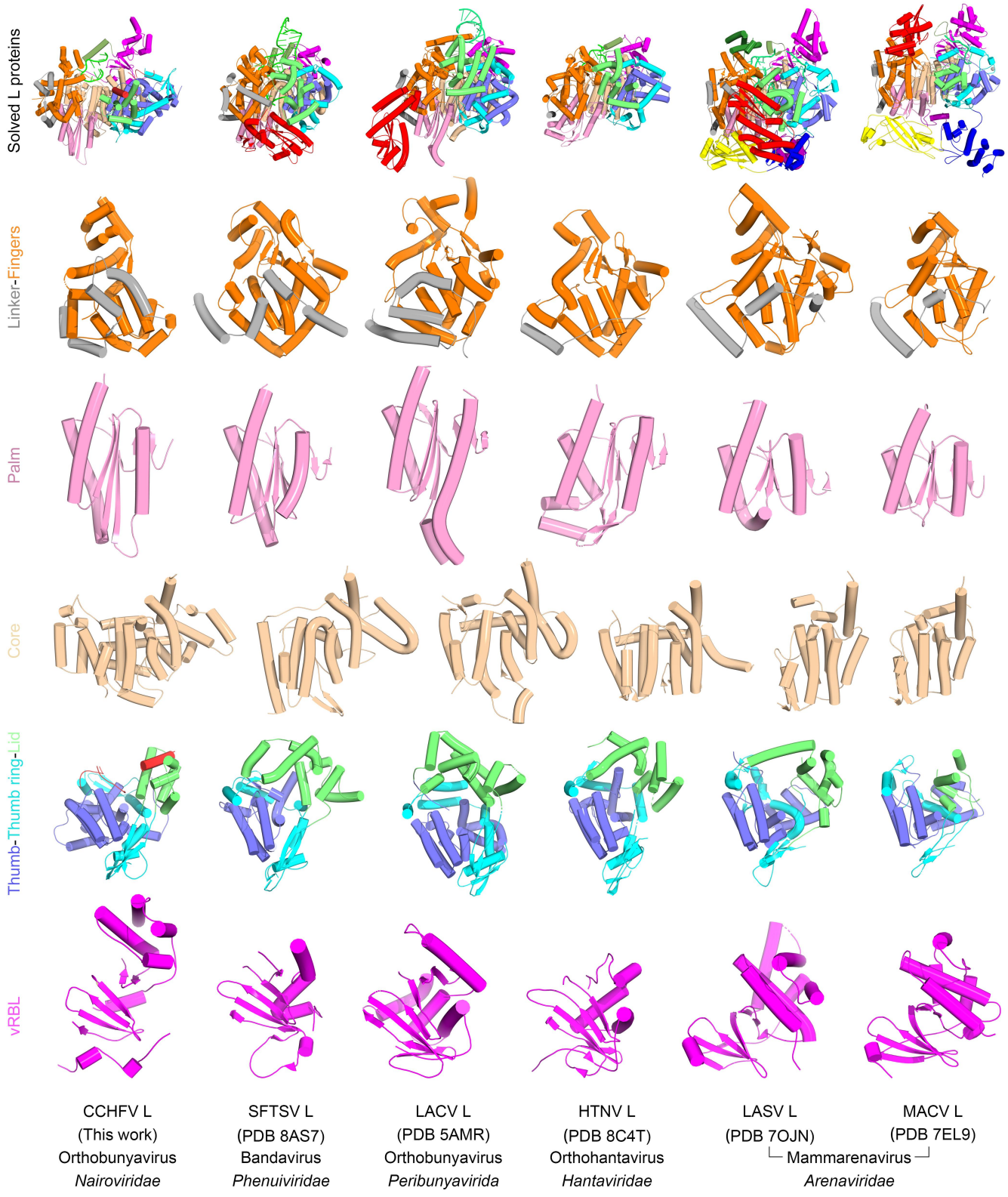

Figure S3. Structural conservation of L proteins across the Bunyavirales order, related to Figure 2
Structural comparison of the CCHFV L protein (this work) with representative polymerases from the *Bunyavirales* order: SFTSV (*Bandavirus;* PDB 8AS7), LACV (*Orthobunyavirus*; PDB 5AMR), HTNV (*Orthohantavirus*; PDB 8C4T), LASV (*Mammarenavirus*; PDB 7OJN) and MACV (*Mammarenavirus*; PDB 7EL9). The top row shows the full structures; subsequent rows display individual domains (Linker–Fingers, Palm, Core, Thumb–Thumb ring–Lid, and vRBL) in identical orientations. The comparison highlights the high degree of structural conservation in the core machinery despite sequence divergence.

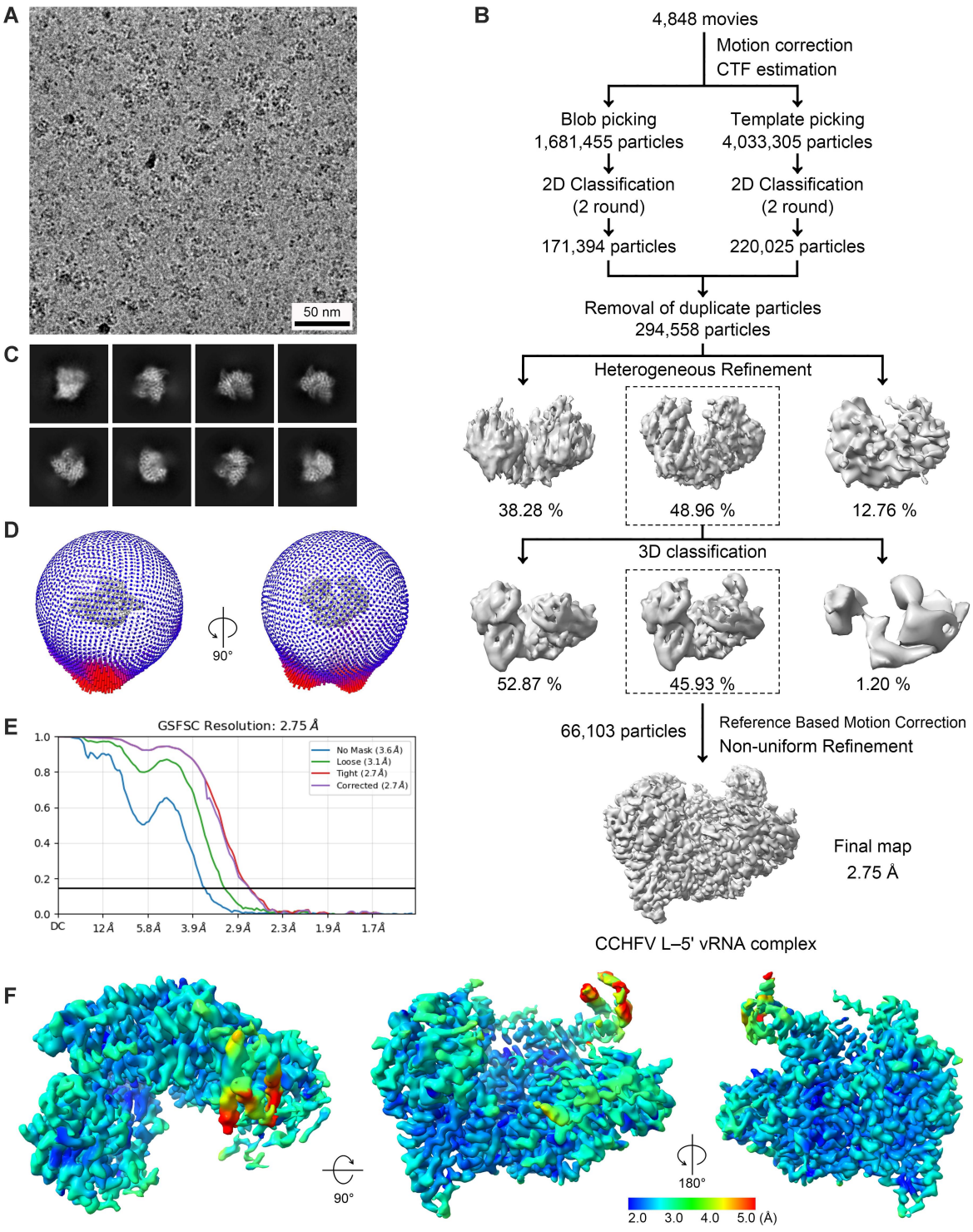

Figure S4. Cryo-EM data processing and reconstruction of the CCHFV L–5' vRNA complex, related to Figure 3

(A) Representative cryo-EM micrograph of the CCHFV L–5' vRNA complex. Scale bar, 50 nm.

(B) Data processing workflow. Particles were picked from 4,848 movies using blob and template-based strategies, followed by multiple rounds of 2D classification, heterogeneous refinement and 3D classification. Non-uniform refinement of 66,103 particles yielded a final map at 2.75 Å resolution.

(C) Representative 2D class averages.

(D) Angular distribution of the particles used for the final reconstruction.

(E) Gold-standard FSC curves indicating a final global resolution of 2.75 Å based on the FSC = 0.143 criterion.

(F) Local resolution map of the final reconstruction shown in three distinct views, presented in the same orientations as Figures 1B and 1C; the resolution color key is shown below.

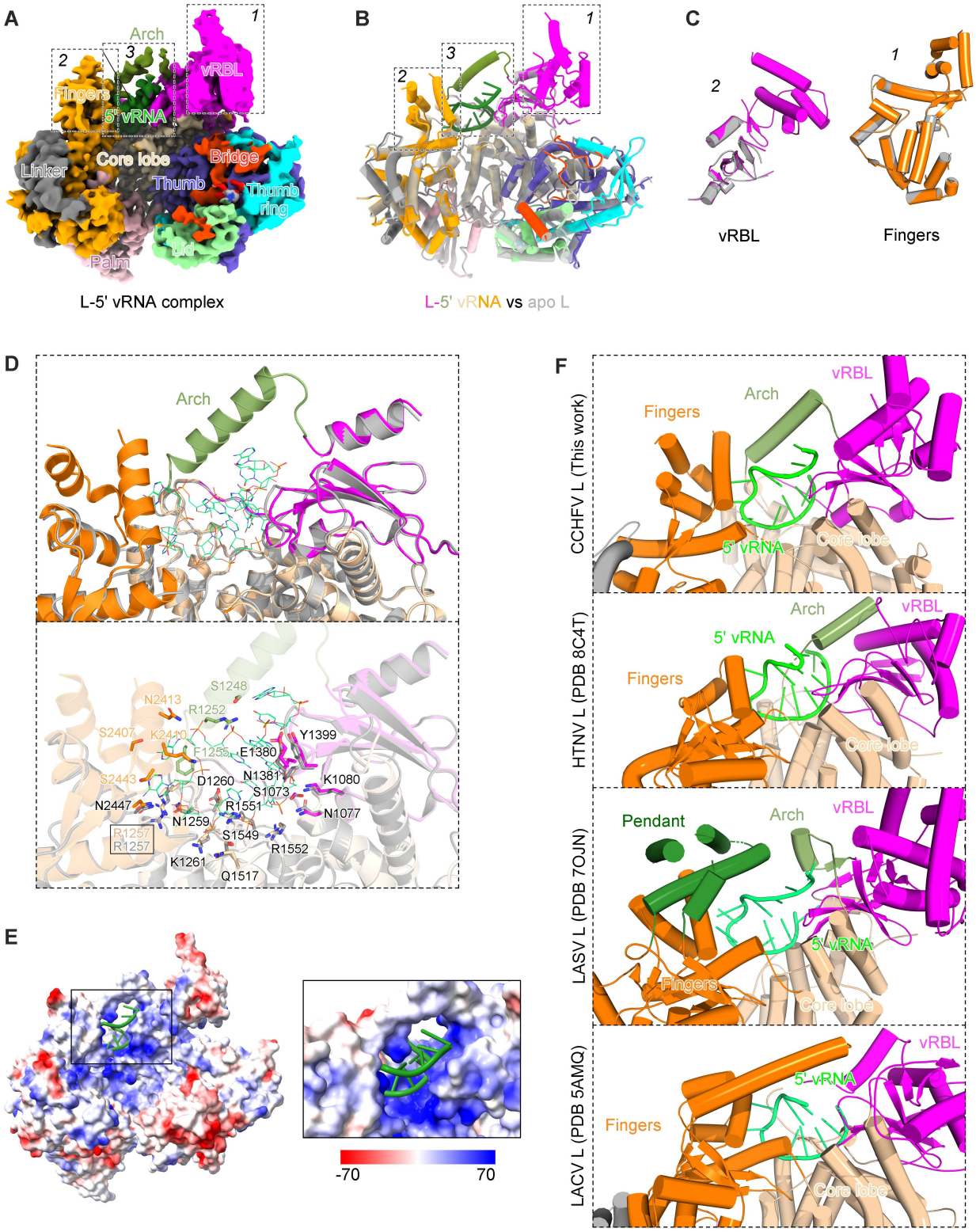
A
Arch
1
2
3
vRBL
Fingers
5' vRNA
Linker
Core lobe
Bridge
Thumb
Thumb ring
Lid
Palm
L-5' vRNA complex
B
1
3
2
L-5' vRNA vs apo L
C
2
1
vRBL
Fingers
D
Arch
S1248
N2413
R1252
S2407
K2410
Y1399
F1255
E1380
S2443
D1260
N1381
K1080
S1073
N2447
R1551
N1077
N1259
S1549
R1257
R1257
R1552
K1261
Q1517
E
-70
70
F
CCHFV L (This work)
vRBL
Arch
Fingers
5' vRNA
Core lobe
HTNV L (PDB 8C4T)
Arch
vRBL
5' vRNA
Fingers
Core lobe
LASV L (PDB 7OJN)
Pendant
Arch
vRBL
5' vRNA
Fingers
Core lobe
LACV L (PDB 5AMQ)
vRBL
5' vRNA
Fingers
Core lobe

Figure S5. Structural analysis of the CCHFV L–5' vRNA complex, related to Figure 3

(A) Cryo-EM density map of the L-5' vRNA complex.

(B) Superposition of the atomic models of the apo (gray) and 5' vRNA-bound (colored by domain) states. Regions exhibiting significant structural differences—the vRBL (1), Fingers (2) and Arch (3) domains—are highlighted with dashed boxes in (A) and (B).

(C) Structural superposition of the vRBL (magenta) and Fingers (orange) domains from the RNA-bound state with the apo state (gray), highlighting the stabilization of flexible regions upon RNA binding.

(D) Detailed comparison of the 5' vRNA binding pocket. Top: overall structural alignment of the 5' vRNA-bound (colored, opaque) and apo (gray, transparent) states. Bottom: close-up view of the key residues involved in vRNA binding. Side chains of interacting residues are shown as sticks and labeled; the RNA is shown as lime lines.

(E) Electrostatic potential surface of the CCHFV L protein. The RNA-binding site is outlined with a solid black box and shown in the zoomed-in view . The 5' vRNA is depicted as a green cartoon. The electrostatic potential scale bar is shown below.

(F) Structural comparison of the 5' vRNA binding pocket in CCHFV (this work) with HTNV (PDB 8C4T), LASV (PDB 7OJN), and LACV (PDB 5AMQ). The comparison demonstrates the conservation of the 5' vRNA binding mechanism across the *Bunyavirales* order. All structures are colored according to the CCHFV domain definitions, except for the unique pendant domain in LASV (colored forest green).

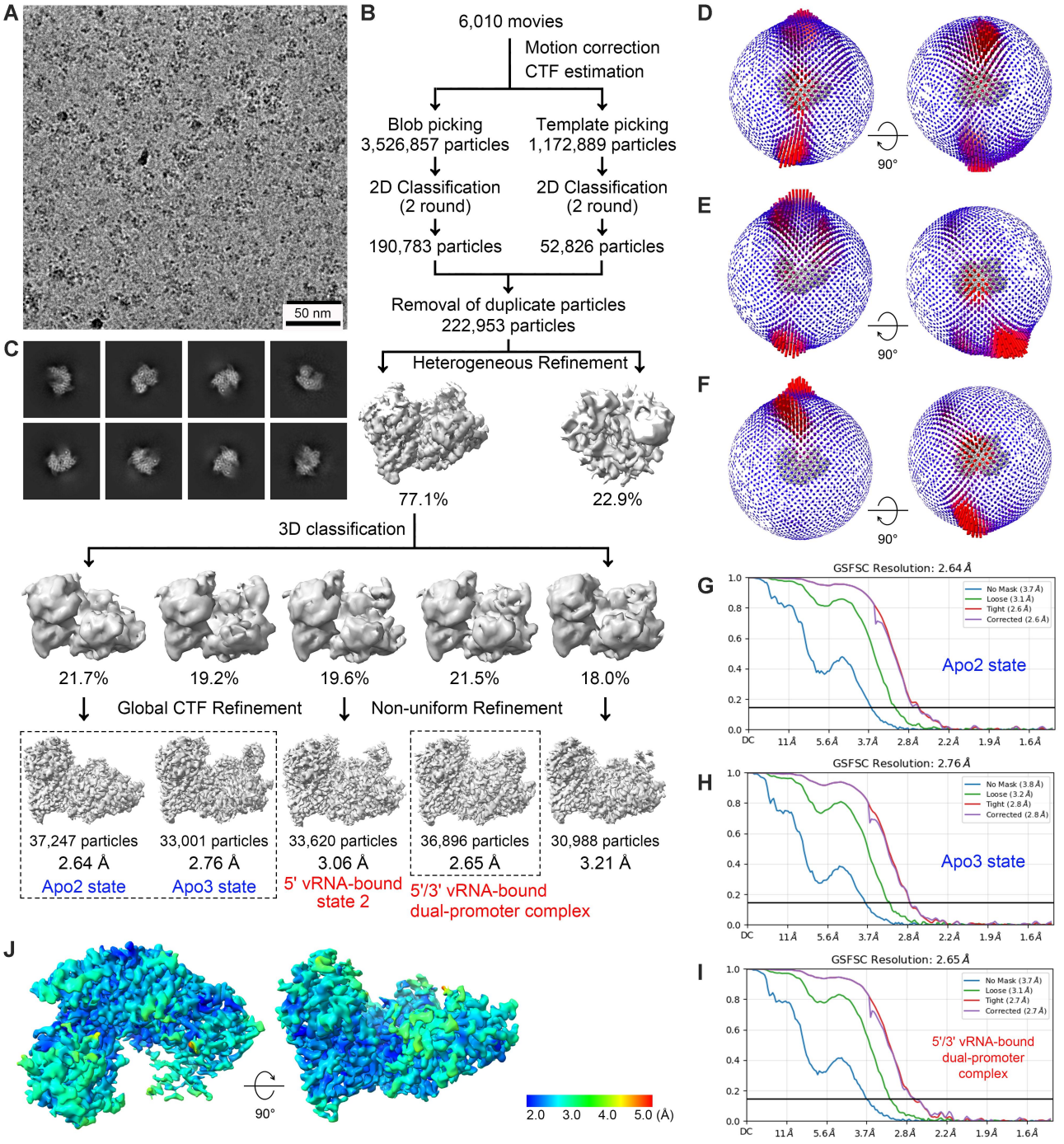
A
50 nm
B
6,010 movies
Motion correction
CTF estimation
Blob picking
3,526,857 particles
Template picking
1,172,889 particles
2D Classification
(2 round)
2D Classification
(2 round)
190,783 particles
52,826 particles
Removal of duplicate particles
222,953 particles
Heterogeneous Refinement
77.1%
22.9%
C
3D classification
21.7%
19.2%
19.6%
21.5%
18.0%
Global CTF Refinement
Non-uniform Refinement
37,247 particles
2.64 Å
Apo2 state
33,001 particles
2.76 Å
Apo3 state
33,620 particles
3.06 Å
5' vRNA-bound
state 2
36,896 particles
2.65 Å
5'/3' vRNA-bound
dual-promoter complex
30,988 particles
3.21 Å
D
90°
E
90°
F
90°
G
GSFSC Resolution: 2.64 Å
No Mask (3.7 Å)
Loose (3.1 Å)
Tight (2.6 Å)
Corrected (2.6 Å)
Apo2 state
H
GSFSC Resolution: 2.76 Å
No Mask (3.8 Å)
Loose (3.2 Å)
Tight (2.8 Å)
Corrected (2.8 Å)
Apo3 state
I
GSFSC Resolution: 2.65 Å
No Mask (3.7 Å)
Loose (3.1 Å)
Tight (2.7 Å)
Corrected (2.7 Å)
5'/3' vRNA-bound
dual-promoter
complex
J
90°
2.0 3.0 4.0 5.0 (Å)
K
90°
L
90°

Figure S6. Cryo-EM data processing and reconstruction of the CCHFV L–dual-promoter complex dataset, related to Figure 4

(A) Representative cryo-EM micrograph of the CCHFV L–dual-promoter complex sample. Scale bar, 50 nm.

(B) Cryo-EM data processing workflow. A total of 6,010 movies were subjected to motion correction and CTF estimation. Particles were initially identified using both blob picking (3,526,857 particles) and template-based picking (1,172,889 particles). Following two rounds of 2D classification and duplicate removal, 222,953 particles were retained. Subsequent heterogeneous refinement and 3D classification revealed multiple functional states. Further processing using global CTF and non-uniform refinement yielded high-resolution maps for the Apo2 state (37,247 particles; 2.64 Å), Apo3 state (33,001 particles; 2.76 Å), 5' vRNA-bound state 2 (33,620 particles; 3.06 Å), and the 5'/3' vRNA-bound dual-promoter complex (36,896 particles; 2.65 Å).

(C) Representative 2D class averages showing various orientations within the dataset.

(D–F) Angular distribution plots for the final reconstructions of the Apo2 state (G), Apo3 state (H), and the dual-promoter complex (I). Red cylinders indicate orientations with higher particle counts.

(G–I) Global resolutions were determined to be 2.64 Å for the Apo2 state (J), 2.76 Å for the Apo3 state (K), and 2.65 Å for the dual-promoter complex (L), based on the gold-standard FSC = 0.143 criterion.

(J–L) Local resolution maps for the Apo2 state (D), Apo3 state (E), and the dual-promoter complex (F). The resolution color key (2.0–5.0 Å) is shown.

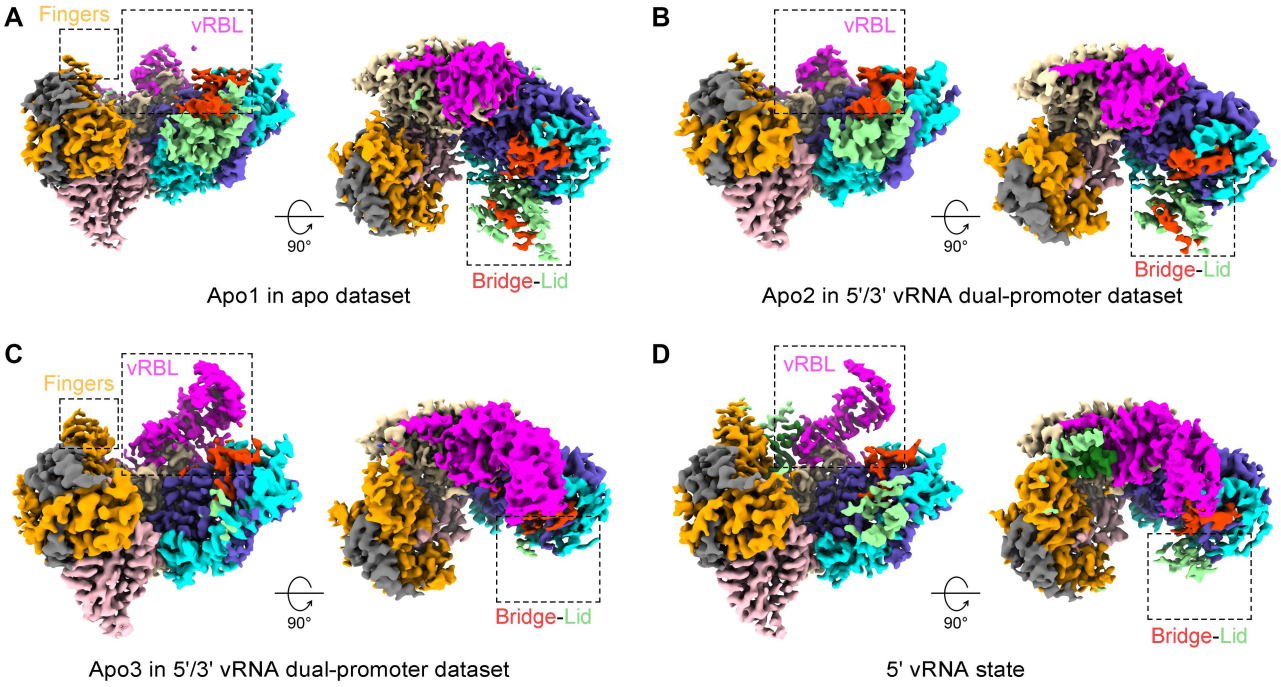

Figure S7. Comparison of multiple apo-state conformations of the CCHFV L protein, related to Figure 7

(A) Apo state (Apo1) from the apo dataset. This represents the baseline "open" conformation in the absence of RNA, characterized by high flexibility in the vRBL and Fingers domains.

(B) Apo2 state from the 5'/3' vRNA dataset. Despite the presence of vRNA in the sample, the Apo2 density is nearly identical to that of Apo1 (A).

(C) Apo3 state from the 5'/3' vRNA dataset. This class captures a transiently "pre-primed" or "pre-activated" conformation. Even without assigned promoter density, the vRBL and Fingers in Apo3 exhibit increased order and stability, shifting toward the conformation observed in the 5' vRNA-bound state, while the Lid–Bridge domains tend toward destabilization.

(D) 5' vRNA-bound state. Shown for comparison with Apo2 and Apo3 to illustrate the ordering of the vRBL and Fingers, as well as the destabilization of the Lid–Bridge domains in the presence of the promoter. The simultaneous identification of the "open" Apo2 and the "primed" Apo3 within the same dataset provides direct structural evidence for a pre-existing conformational equilibrium. This supports an induced-fit model in which 5' vRNA binding stabilizes a specific, ordered conformation from a dynamic ensemble to initiate the "activation-before-loading" pathway. All maps are shown in two orthogonal views and colored by domain; dashed boxes highlight key regions of conformational transition.

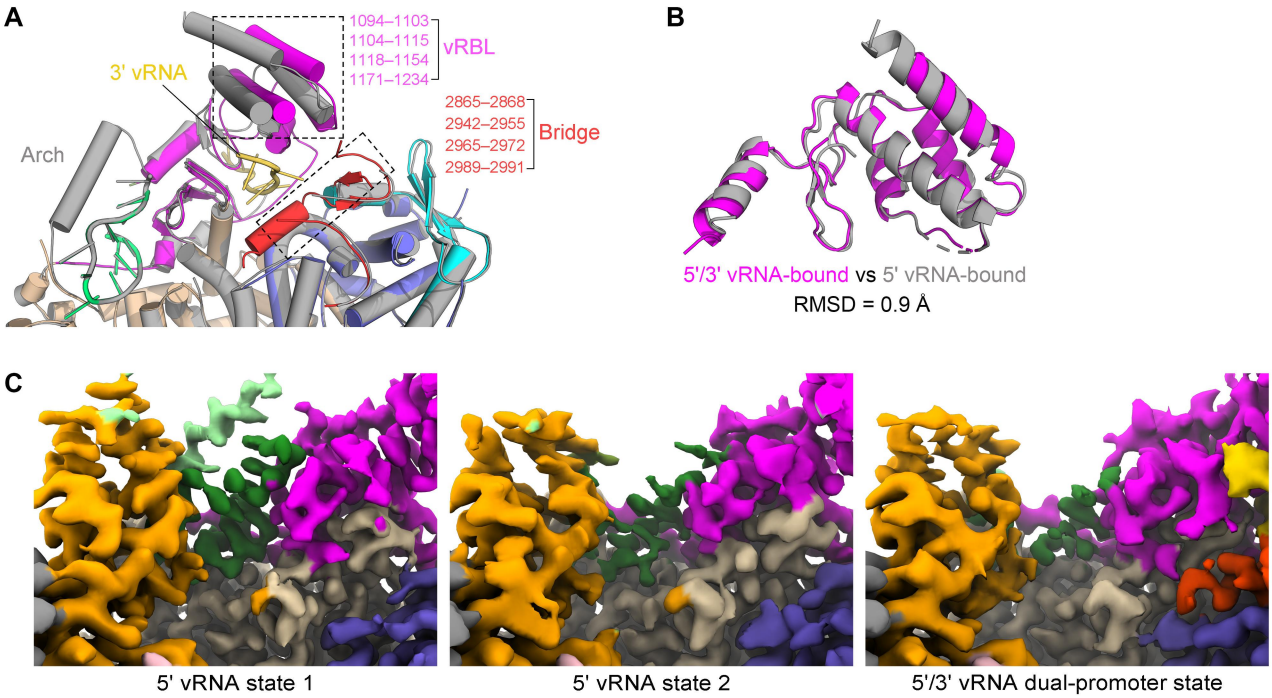

Figure S8. Conformational changes in CCHFV L polymerase upon 3' vRNA binding, related to Figure 4

(A) Superimposition of the 5'/3' vRNA-bound state (domain-colored) and the 5' vRNA-bound state (colored gray), with key regions highlighted. Conformational changes are primarily observed in the vRBL and Bridge (specific residue ranges are indicated), and the Arch (which is stabilized only in the 5' vRNA-bound state). The 3' vRNA (yellow) is positioned within its secondary channel. Dashed boxes highlight the principal conformational changes in the vRBL and Bridge.

(B) Structural superposition of the vRBL domain between the 5' vRNA-bound state (gray) and the 5'/3' vRNA-bound state (magenta). An RMSD of 0.9 Å indicates that the vRBL domain maintains a stable fold and undergoes only a rigid-body rotation during the transition from the 5' vRNA-bound intermediate to the dual-promoter complex.

(C) Conformational dynamics of the 5' vRNA template. Comparison of the cryo-EM densities for the 5' vRNA (forest green) reveals structural variations among three states: a well-resolved, hook-like conformation in the 5' vRNA-bound state 1 (left), a flexible, partially diffuse density in state 2 (middle) and the dual-promoter complex (right). These variations highlight the dynamic conformational equilibrium of the enzyme.

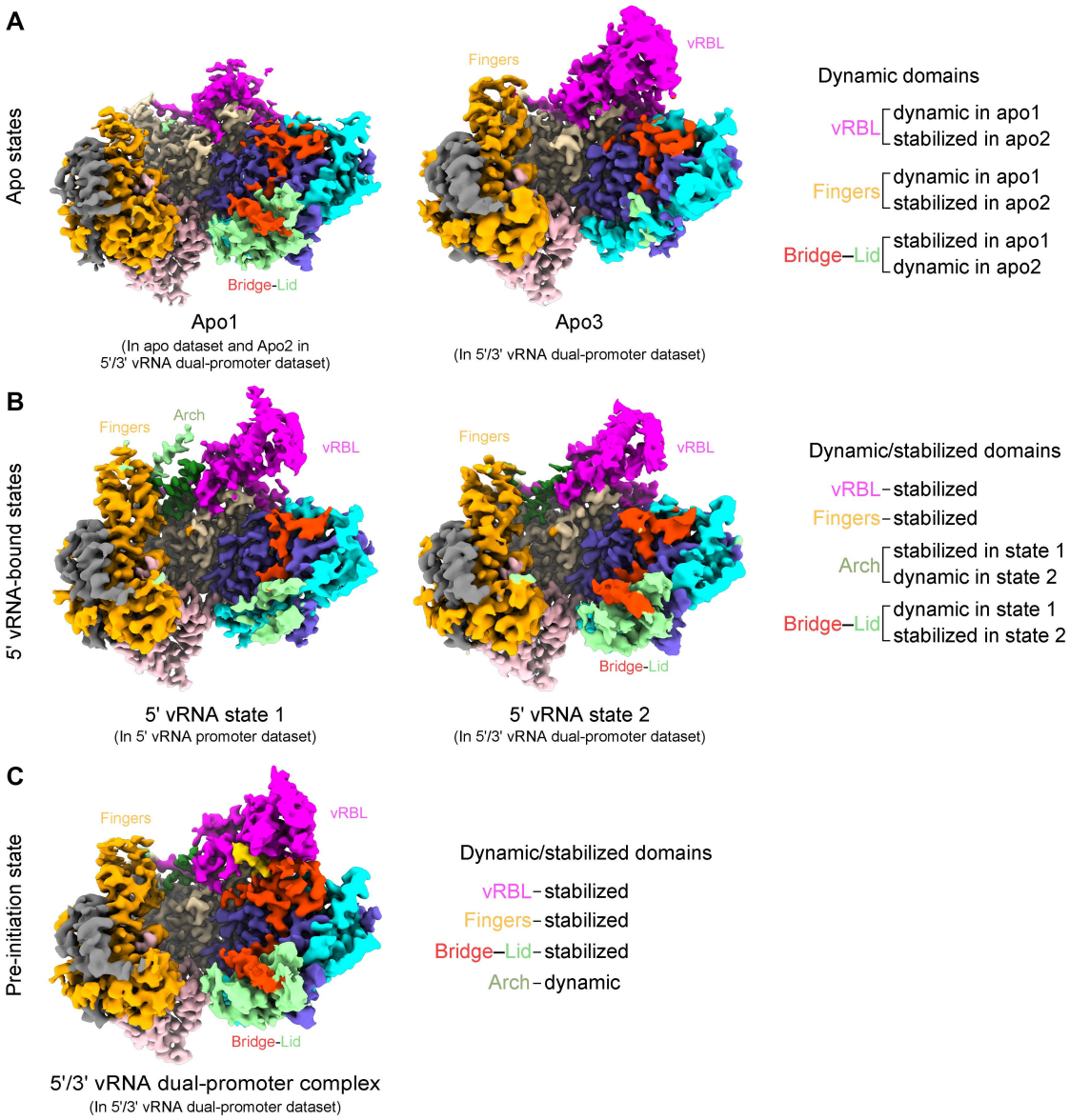

Figure S9. Conformational dynamics and domain stabilization of the CCHFV L protein across different states, related to Figures 4 and 7

(A) Apo states. Apo1 (left; derived from the apo dataset and the Apo2 class in the 5'/3' vRNA dataset) and Apo3 (right; from the 5'/3' vRNA dataset). In Apo1, the vRBL and Fingers domains are dynamic, while the Bridge–Lid region is stabilized. In contrast, Apo3 exhibits stabilized vRBL and Fingers domains, whereas the Bridge–Lid region becomes dynamic.

(B) 5' vRNA-bound states. 5' vRNA state 1 (left; from the 5' vRNA promoter dataset) and 5' vRNA state 2 (right; from the 5'/3' vRNA dual-promoter dataset) (right). Both states show stabilized vRBL and Fingers. The Arch domain is stabilized in state 1 but dynamic in state 2. Conversely, the Bridge–Lid region is dynamic in state 1 and stabilized in state 2.

(C) Pre-initiation state. The 5'/3' vRNA dual-promoter complex represents the pre-initiation assembly. In this state, the vRBL, Fingers, and Bridge–Lid domains are all stabilized, while the Arch domain remains dynamic.

CCHFV L protein structures are shown as cryo-EM density maps colored by domains. The stabilization and mobilization of specific domains (vRBL, Fingers, Arch, and Bridge–Lid) characterize the stepwise assembly of the dual-promoter complex, highlighting the intrinsic plasticity of the CCHFV L protein during promoter recognition.

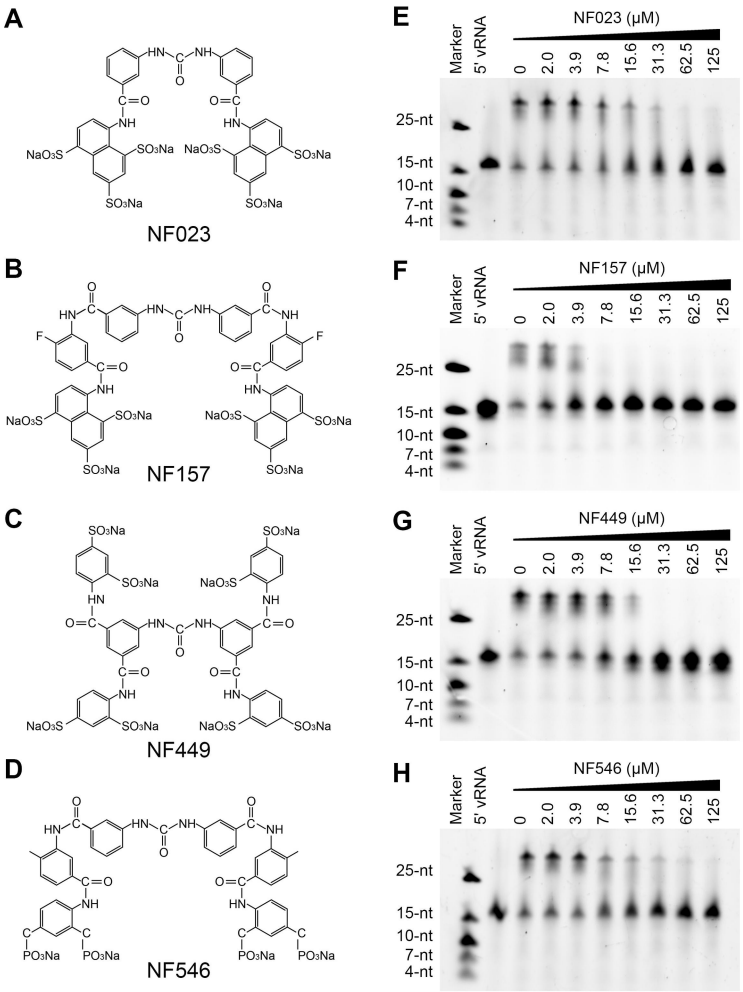

Figure S10. Inhibitory activity of suramin analogues against the CCHFV L protein, related to Figure 5
(A–D) Chemical structures of suramin analogues evaluated to explore suramin as an optimizable chemical scaffold. The structures shown include NF023 (A), NF157 (B), NF449 (C), and NF546 (D).
(E–H) *In vitro* polymerase activity assays of suramin analogues. Concentration-dependent inhibition of CCHFV RdRp activity was evaluated via primer-extension assays for NF023 (E), NF157 (F), NF449 (G), and NF546 (H). The tested analogues exhibit varying degrees of enzymatic suppression: NF157 retains inhibitory activity comparable to that of suramin; NF449 shows a slightly reduced but evident inhibitory effect; NF023 and NF546 exhibit significantly diminished inhibitory activities. Data are representative of at least three independent experiments.

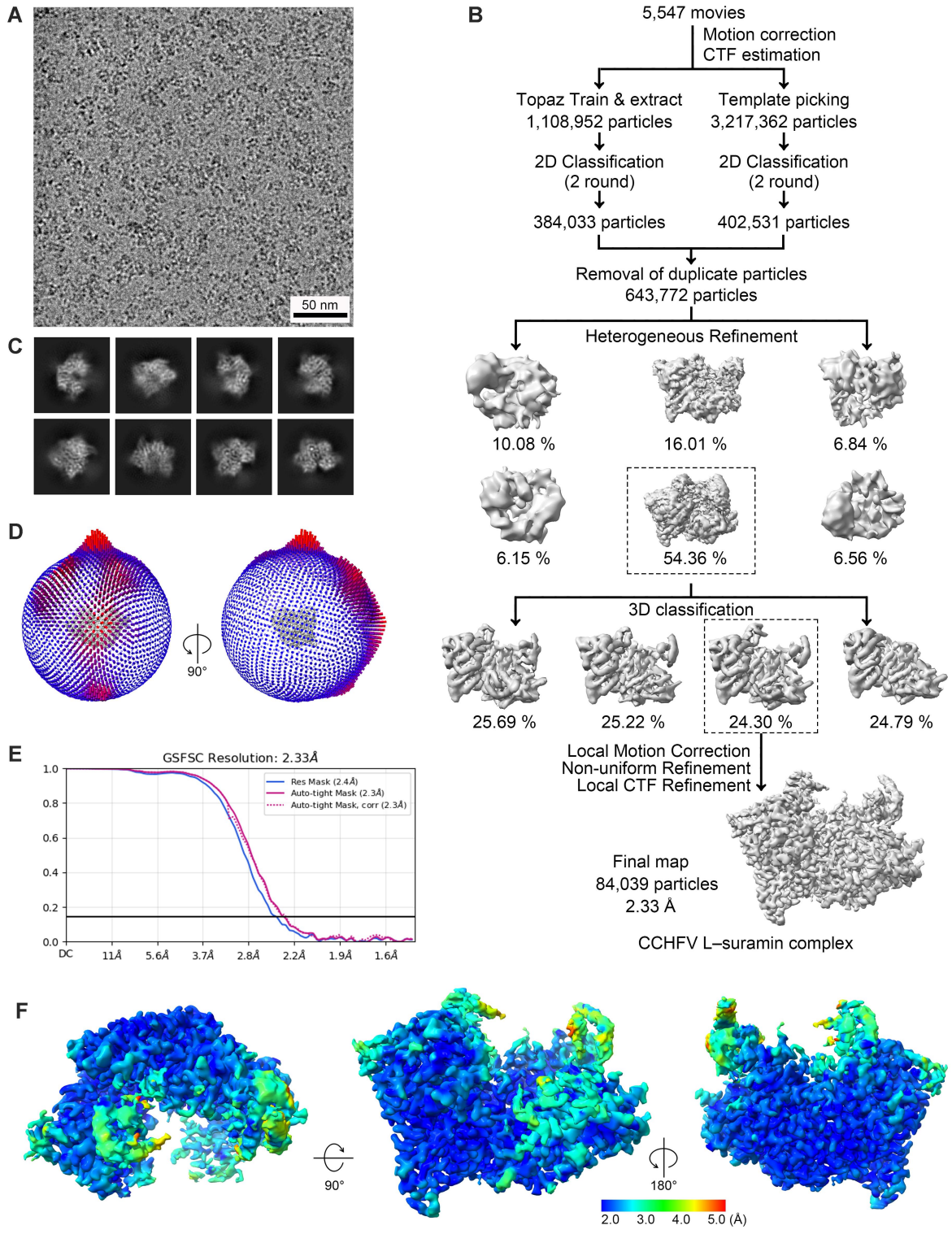

Figure S11. Cryo-EM data processing and reconstruction of the CCHFV L–suramin complex, related to Figure 5

(A) Representative cryo-EM micrograph of the CCHFV L–suramin complex. Scale bar, 50 nm.

(B) Workflow of cryo-EM data processing. Particles were picked from 5,547 movies using Topaz and template-based strategies. Following 2D classification, heterogeneous refinement and 3D classification, a final set of 84,039 particles was subjected to non-uniform refinement, reference based motion correction, and local CTF refinement, yielding a density map at a global resolution of 2.33 Å.

(C) Representative 2D class averages of the L–suramin complex particles.

(D) Angular distribution of the particles used in the final reconstruction.

(E) Gold-standard FSC curves indicating a final global resolution of 2.33 Å at the FSC = 0.143 threshold.

(F) Local resolution map of the final reconstruction shown in three distinct views, presented in the same orientations as **Figures 1**B and **1**C; the resolution color key is provided below.

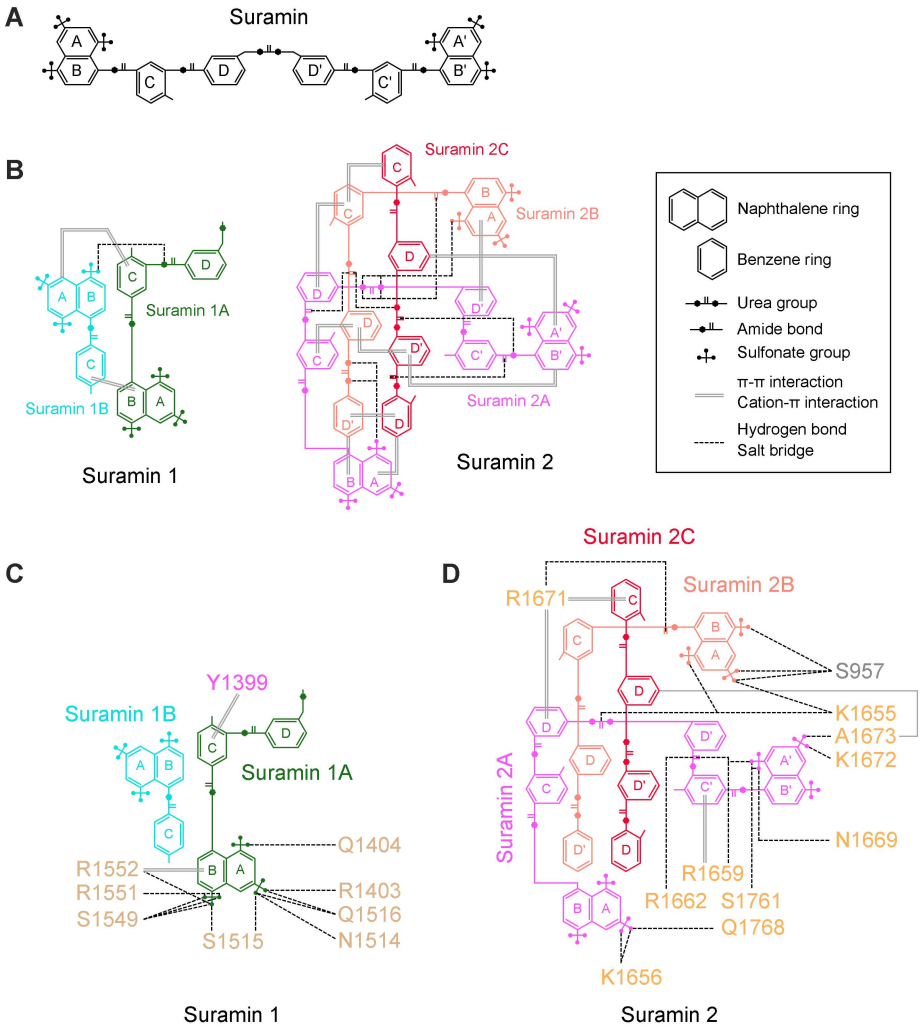

Figure S12. Schematic representation of interactions in the CCHFV L–suramin complex, related to Figures 5 and 6

(A) Chemical structure of the symmetrical suramin molecule. The naphthalene (A, B) and benzene (C, D) rings are labeled; primes (') denote the corresponding rings on the symmetrical moiety.

(B) Intermolecular interactions within suramin assemblies. Left: Site 1 (Suramin 1), showing interactions within the suramin dimer. Right: Site 2 (Suramin 2), showing interactions within the suramin trimer assembly.

(C–D) Schematic representations of interactions between the L protein and suramin assemblies. Only residues involved in direct interactions are shown. Hydrogen bonds and salt bridges are indicated by black dashed lines. π–π interactions (in B) and cation–π interactions (in panels C and D) are depicted as gray double lines. The coloring of suramin molecules and protein residues is consistent with the main text figures.

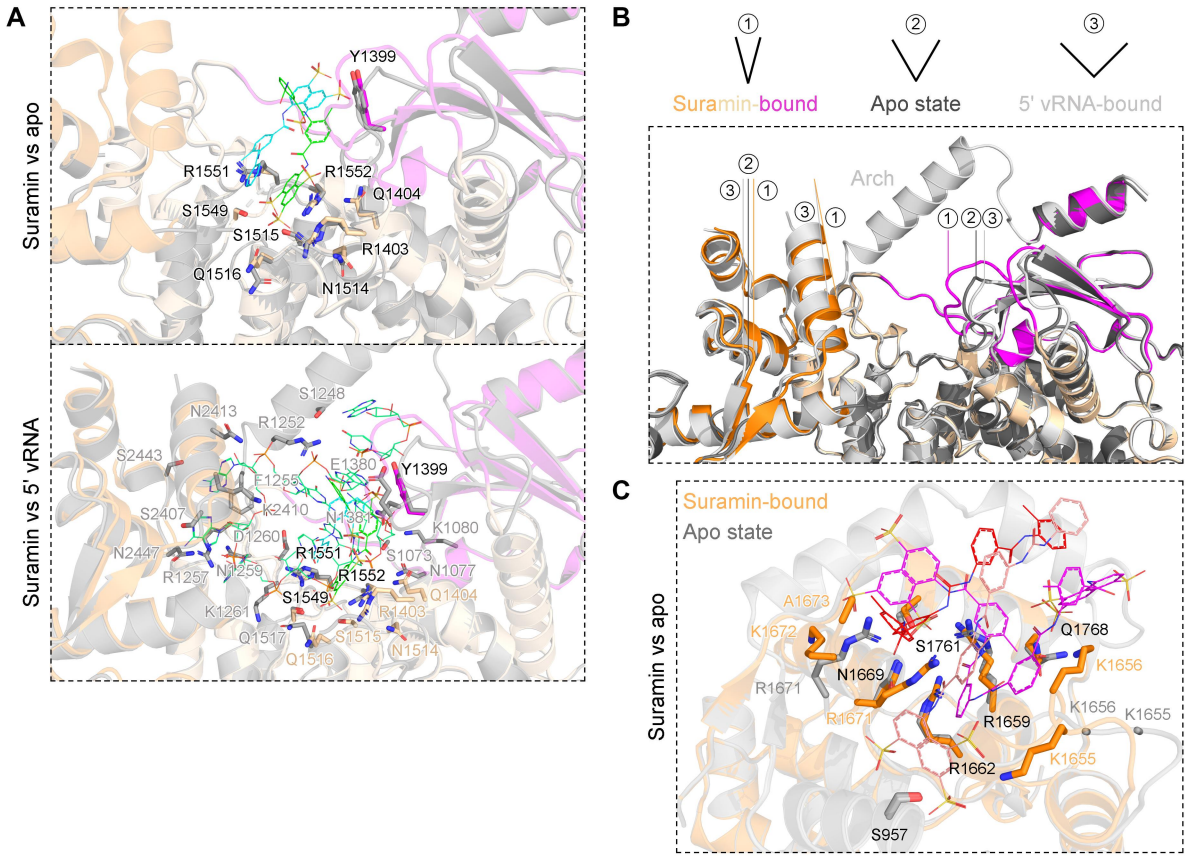

Figure S13. Conformational analysis of residues at the suramin–L protein interface, related to Figure 6

(A) Structural superposition of the suramin-bound state with the apo state (top) and the RNA-bound state (bottom) at Site 1 (Suramin 1). Residues 1373-1380 undergoes a significant conformational shift, pulling its hosting loop towards the inhibitor, while other binding residues exhibit minimal structural changes. Notably, the bottom panel confirms that suramin physically occupies the RNA-binding pocket, creating severe steric clashes. Residues Y1399, S1549, R1551, and R1552 are shared recognition residues for both suramin and the 5' vRNA.

(B) Structural superposition of the suramin-bound (colored), apo (black), and 5' vRNA-bound (gray) states. Relative to the apo state, RNA binding induces a slight expansion of the architecture, whereas suramin binding causes contraction. Labels 1–3 indicate the relative positions of the same site in the suramin-bound, apo and RNA-bound states, respectively.

(C) Structural superposition at Site 2 (Suramin 2). Suramin binding stabilizes K1672 and A1673 while inducing conformational shifts in K1655, K1656 and R1671. Specifically, the engagement of K1655 and K1656 triggers a loop shift towards the drug; other interfacial residues remain largely unchanged.

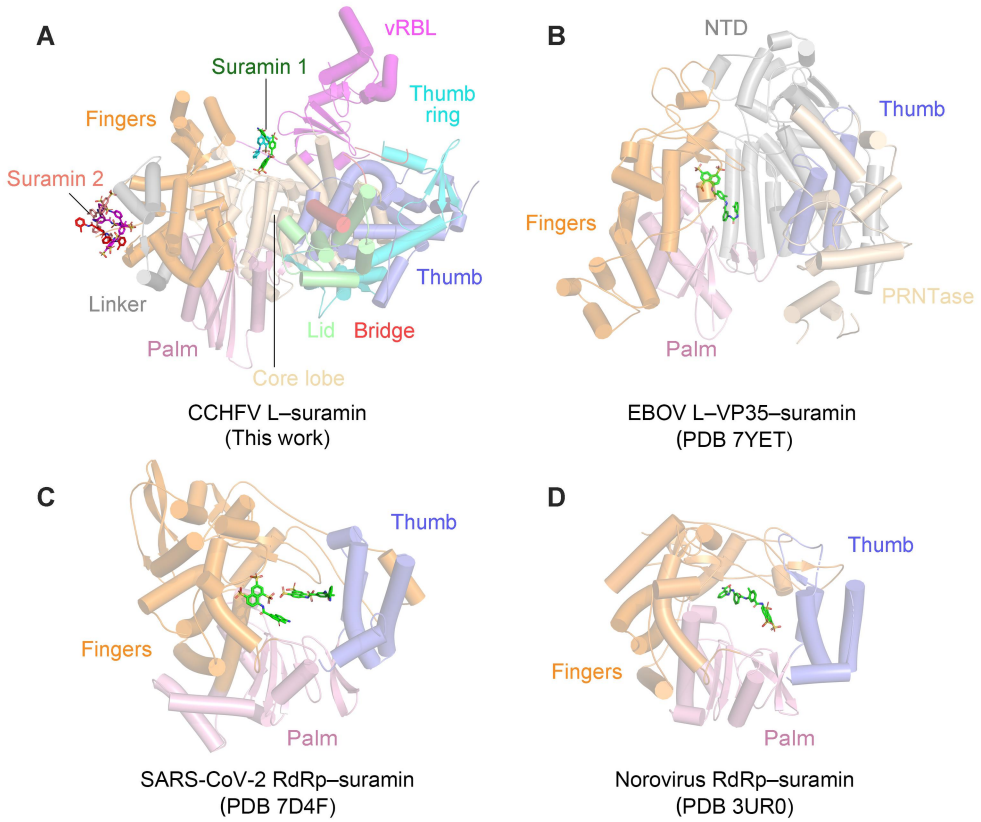

Figure S14. Comparison of suramin binding and inhibition mechanisms across viral RNA polymerases, related to Figures 6 and 7

(A) CCHFV L–suramin complex (this work). Suramin utilizes dual binding sites: Site 1 within the 5' vRNA-binding pocket and Site 2 on the exterior surface of the Linker–Fingers domains.

(B) Ebola virus (EBOV) L–VP35 polymerase complex (PDB 7YET). Suramin binds within the NTP entry channel, physically blocking the entry of substrates into the active site.

(C) SARS-CoV-2 RdRp (PDB 7D4F). Two suramin molecules bind within the catalytic chamber, blocking the binding of both template and primer RNA strands.

(D) Norovirus RdRp (PDB 3UR0). Suramin binds in the cleft between the Fingers and Thumb domains, preventing the positioning of the RNA template for initiation. The binding sites and inhibitory mechanism in CCHFV are distinct from the active-site or channel-blocking mechanisms reported for other viral polymerases. Proteins are shown as transparent cartoons (colored by domain to match the CCHFV structure); suramin is shown as green sticks.

Table S1. Cryo-EM statistics for the CCHFV L protein in apo and promoter/inhibitor-bound complexes, related to Figures 1, 3, 5 and STAR Methods

	CCHFV L protein alone	CCHFV L–5' vRNA complex	CCHFV L–suramin complex
	EMD-68655 PDB 22TE	EMDB-68663 PDB 22TR	EMD-68657 PDB 22TH
Data collection and processing			
Microscope		Titan Krios G4	
Detector		Falcon 4	
Magnification (nominal/calibrated)		165,000	
Voltage (kV)		300	
Electron exposure ($e^-/Å^2$)		50	
Defocus rang (μm)		–0.8~–2.5	
Pixel size (Å)		0.73	
Symmetry imposed		C1	
Initial particle images (no.)	3,444,016	4,033,305	3,018,770
Final particle images (no.)	48,496	66,103	84,039
Map resolution (Å)	2.59	2.75	2.33
FSC threshold	0.143	0.143	0.143
Map resolution range (Å)	2.5~4.5	2.5~4.5	2.5~4.5
Model refinement and validation			
Initial model used		AlphaFold-predicted model	
Model resolution (Å)	2.9	3.1	2.5
FSC threshold	0.5	0.5	0.5
Model composition			
Chains	1	2	1
Non-hydrogen atoms	10926	12007	11971
Protein residues	1386	1517	1517
Nucleotides	-	11	-
Ligands	2 (Zn^{2+}), 1 Mn^{2+}, 1 Mg^{2+}	2 (Zn^{2+}), 1 Mn^{2+}, 1 Mg^{2+}	2 (Zn^{2+}), 1 Mn^{2+}, 1 Mg^{2+}, 5 (Suramin)
***B* factors ($Å^2$)**			
Protein	43.74	58.59	67.59
Nucleotides	-	22.17	-
Ligand	100.93	93.15	129.54
R.m.s. deviations			
Bond lengths (Å)	0.002	0.002	0.002
Bond angles (°)	0.499	0.489	0.452
Validation			
MolProbity score	1.42	1.56	1.49
Clash score	7.16	7.83	7.33
Rotamer outliers (%)	0.65	0.15	0.85
Ramachandran plot			
Favored (%)	97.87	97.31	97.59
Allowed (%)	2.13	2.69	2.35
Disallowed (%)	0.00	0.00	0.07

Table S2. Cryo-EM statistics of various conformational states from the dual-promoter dataset, related to Figure 4 and STAR Methods

	L apo2 state	L apo3 state	L–5' vRNA state 2	L–5'/3' vRNA complex
	EMD-80710 PDB 26KD	EMDB-80708 PDB 26KB	EMD-80707 PDB 26KA	EMD-80706 PDB 26JZ
Data collection and processing				
Microscope	Titan Krios G4			
Detector	Falcon 4			
Magnification (nominal/calibrated)	165,000			
Voltage (kV)	300			
Electron exposure (e^-/Å^2)	50			
Defocus rang (μm)	–0.8~–2.5			
Pixel size (Å)	0.73			
Symmetry imposed	C1			
Initial particle images (no.)	222,952			
Final particle images (no.)	37,247	33,001	33,620	36,896
Map resolution (Å)	2.64	2.76	3.06	2.65
FSC threshold	0.143	0.143	0.143	0.143
Map resolution range (Å)	2.5~4.5	2.5~4.5	2.5~4.5	2.5~4.5
Model refinement and validation				
Initial model used	AlphaFold-predicted model			
Model resolution (Å)	2.64	2.76	3.03	3.04
FSC threshold	0.5	0.5	0.5	0.5
Model composition				
Chains	1	1	2	3
Non-hydrogen atoms	10653	10,699	11,895	12,727
Protein residues	1359	1,373	1,503	1,572
Nucleotides	-	-	10	18
Ligands	2 Zn^{2+}, 1 Mn^{2+}, 1 Mg^{2+}	2 Zn^{2+}, 1 Mn^{2+}, 1 Mg^{2+}	2 Zn^{2+}, 1 Mn^{2+}, 1 Mg^{2+}	2 Zn^{2+}, 1 Mn^{2+}, 1 Mg^{2+}
***B* factors (Å^2)**				
Protein	77.75	85.09	99.16	73.35
Nucleotides	-	-	56.77	40.12
Ligand	111.11	117.97	114.11	85.89
R.m.s. deviations				
Bond lengths (Å)	0.003	0.002	0.002	0.004
Bond angles (°)	0.485	0.470	0.469	0.549
Validation				
MolProbity score	1.73	1.53	1.65	1.67
Clash score	10.09	7.90	7.86	8.57
Rotamer outliers (%)	0.08	0.25	0.23	0.07
Ramachandran plot				
Favored (%)	96.70	97.54	96.60	96.71
Allowed (%)	3.30	2.39	3.27	3.23
Disallowed (%)	0.00	0.07	0.14	0.06